A Dynamic Spatial-time Dark Level Correction Approach for Lunar Radiometric Calibration of LOIS

LINGPING AN,[1,2] YIHAO WANG,[1,2] HANG ZHAO,[1,2] CAN YU,[1,2] YANHENG WANG,[1,2] SHUANG WANG[1,*] XUEBIN LIU,[1]

[1] *Xi'an Institute of Optics and Precision Mechanics, Chinese Academy of Sciences, Xi'an, Shaanxi 710119, China*
[2] *University of Chinese Academy of Sciences, Beijing 100049, China*
*Corresponding author: wangshuang@opt.ac.cn

Lunar radiometric calibration is used to solve the problem of consistent radiometric calibration for multiple satellite platforms and remote sensors. However, the dark level will fluctuate when observing the Moon with the short-wave infrared spectrometer, which seriously affects the accuracy of the lunar radiation data. In this work, we proposed a dynamic spatial-time dark level correction approach to address the fluctuation of the dark level. This method employs the cold space signals in space and time dimensions to estimate the dark level for each frame individually and to reduce errors due to environmental variations. Experiments on lunar observations at multiple phase angles were conducted and the dark level correction results demonstrate that our proposed method is effective even in the short-wave infrared, and is also superior to currently existing techniques. For the single-band (1700 nm) image of the full moon, the mean background proportion of the proposed method is 1.00%, which is better than that of static dark correction method (2.25%) and linear dark correction method (5.93%). © 2023 Optica Publishing Group

1. INTRODUCTION

With the considerable waking developments in remote sensing technology, the capacity of satellites to consistently record surface observations has been greatly improved, which extends many applications in the fields of land use investigation [1,2], urban planning [3], change detection [4], disaster management [5], etc. Concomitantly, requirements for remote sensing products have escalated to quantitative applications, which involve from initial target imaging to qualitative analysis [6,7]. To extend these requirements, acquiring high-quality images from parameter-given and regularly calibrated sensors is a prerequisite for succeeding activities of remote sensing. However, consistent radiometric calibration of multiple satellite platforms and remote sensors remains unequivocally challenging for transforming massive data into quantitative products. Among the existing on-orbit calibration methods, lunar calibration attracts more interest since its advantages of low cost and uniformizing the calibration benchmarks for multiple remote sensors [8]. Both the TRUTHS (The Traceable Radiometry Underpinning Terrestrial and Helio Studies) and CLARREO (The Climate Absolute Radiance and Refractivity Observatory) programs referred to lunar calibration and considered the Moon as a calibration reference for long-term observations [9,10]. Spacecraft measurements of the Moon are compared with model results under the same observation

geometry. An accurate photometric model of the Moon is the key to lunar radiometric calibration. Long time series of ground-based lunar observations provide data support for model building. The Robotic Lunar Observatory (ROLO) project has developed a lunar irradiance model in 23 VNIR and 9 SWIR filter bands based on the extensive database of radiance images [11]. All images were processed to the level of top-of-atmosphere irradiance. However, the absolute radiometric accuracy of this model is 5% to 10% which cannot satisfy current requirements for on-orbit calibration [12].

Affected by ambient radiation, electronic noise, observation method, etc., the unstable and heterogeneous background in lunar images makes them hard to directly represent the lunar signal. Thus, building a high-precision lunar image processing whether in the initial imaging stage or final application stage is an indispensable step for lunar calibration.

In lunar imaging, the dark level as the response of a detector in case of lacking illumination, is one of the most seriously influential factors decreasing the imaging quality. While the works of dark level correction, as a step of remote sensing image pre-processing, still have limitations. The correction effect for data in the infrared band is far inferior to those in the visible band. Many factors produce the dark level, including properties of detectors (such as substrate voltage, dark current and noise), and environmental conditions (such as external stray light and ambient temperature fluctuation) [13,14]. Although infrared spectrometers have

temperature-controlled devices, the ambient temperature of the detector will be increased slightly after it reaches a predetermined value [15]. To eliminate the dark level of remote sensing images, some methods have been designed and can be further categorized into three groups: (1) Cold sky signal. Remote sensing images mostly employ a cold sky signal instead of a dark level. Earth satellites regarded the cold sky signal from the space view as equal to the dark level for lunar calibration [16-19]; Wang [20] estimated the dark level of the entire lunar image by partial cold sky signals in observation. These methods all assumed that the dark level of the remote sensor was constant throughout the observation process, and ignored the effect of temperature changes on the dark level. (2) Association model. Dobbins et al. [15] inferred the dark level through temperature, but it still needs laborious pre-experiments to determine the relationships between the dark level and the temperature, as well as the real-time temperature. (3) Collection test. Temperature and integration time affect the dark current and thermal noise of the instrument, especially for detectors with long exposures [21]. Therefore, the dark level must be reacquired when the operating environment and mode change [22]. Lin et al. [23] collected the dark level after scanning at intervals of several wavelengths by controlling the baffle of the light source used in laboratory calibrations. The first group of methods ignores the fluctuation of the dark level influenced by the operating state and stability of the detector. The second and third groups of methods require additional instrumentation and time. Therefore, exploring the methods for eliminating the efforts from the dark level is significant to convenient the applications of lunar radiometric calibration.

To develop an effective dark level correction method without extra equipment, in this work, we proposed a dynamic spatial-time dark level correction method based on the cold sky signal. Without ambient temperature information, our design is constructed entirely from the cold sky signal surrounding the moon. Moreover, selecting cold sky signals at suitable positions is a pivotal step to establish a static model and a changing trend respectively. The correction results of lunar images with different phase angles demonstrate that our dynamic model shows promising performance via modeling dark level dynamically.

We summarize the contributions of our work in three parts:

· We conducted lunar observation experiments during one lunar phase cycle and acquired lunar cubes of hyperspectral data in the short-wave infrared band.

· We proposed a simple yet effective dark level correction model, which obtains the dark level of each frame only from the lunar image.

· We evaluated our dark level correction method using the background proportion metric and compare it with other methods. The results demonstrate that the dynamic dark level model is closest to the true value, and surpasses other methods.

2. OBSERVATION OF LUNAR RADIATION

All lunar observation experiments are conducted based on the Lunar Observation Imaging Spectrometer (LOIS), developed by the Xi'an Institute of Optics and Precision Mechanics, Chinese Academy of Sciences (XIOPM, CAS). LOIS is designed to carry out long time series of automated lunar observations to provide data support for the establishment and refinement of the SWIR lunar high-precision model. As listed in Table 1, LOIS collected lunar radiation data in the short-wave infrared band with a spectral resolution of 8.22 nm. The

physical map of the spectrometer is constructed with three parts - telescopic system, spectroscopic system, and detection system, as shown in Fig. 1. All optical components are surrounded by a blackout hood, which can effectively isolate and absorb external stray light.

Table 1. Main technical parameters of the LOIS

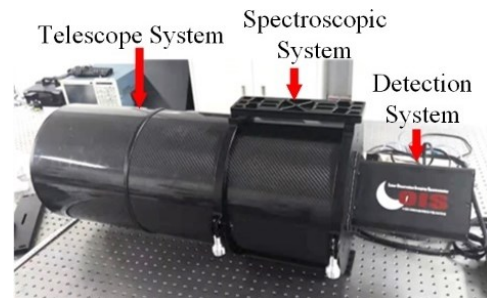| Parameter	Value
Spectral range	1000-2400nm
Spectral resolution	8.22nm
Radiation uncertainty	<3% (k=1)
Instantaneous Field of View (IFOV)	$1° \times 0.002°$
Signal-Noise Ratio	>500

Fig. 1. Physical map of the LOIS. LOIS consists of three parts, including a telescopic system, a spectroscopic system, and a detection system.

The layout of LOIS is presented in Fig. 2. A Ritchey-Chrétien design telescope, slit and PGP (prism-grating-prism) component are attached to a mounting bracket. Behind the mounting bracket the SWIR CMOS detector is attached to the computer used for data acquisition and processing. LOIS utilizes a 500×256 HgCdTe array manufactured by Sofradir. The array pixels have excellent linearity of better than 99.5%. The readout noise for the system is lower than 149 e- (for 0.5 Me- gain) and 339 e- (for 2.5Me- gain).
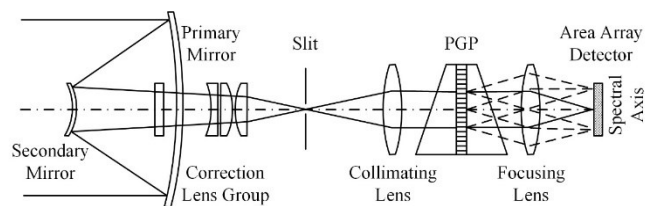

Fig. 2. The layout of LOIS. The light rays pass through A Ritchey-Chrétien design telescope and slit, and are focused on the area array detector after dispersion by the PGP component.

We used an equatorial instrument to support the spectrometer. The equatorial instrument enables arbitrary positioning in space by adjusting the pointing axis and the pitch angle. Fig. 3 illustrates the passive push-broom mode, in which the spectrometer is fixed with the slit direction perpendicular to the lunar trajectory and continuously collects data as the moon passes by [24]. The duration time of imaging collection is far greater than that of the moon occurring in a slit field of view. This ensures that the spectrometer captures complete series of images of the moon. The size of the imaging spectrometer detector area array is W×K, where the W and

K represent the number of spatial pixels and bands respectively. One complete scan can collect L frames of data, and by splicing these data, a data cube of size W×L×K can be obtained. The data cube contains two-dimensional spatial and one-dimensional spectral information, and its formation process is shown in Fig. 4.
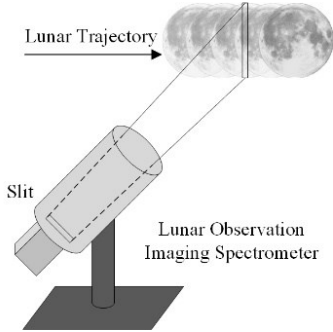

Fig.3. Schematic diagram of the observation mode of LOIS. During the observation, the moon slid through the slit of LOIS by its orbital motion.
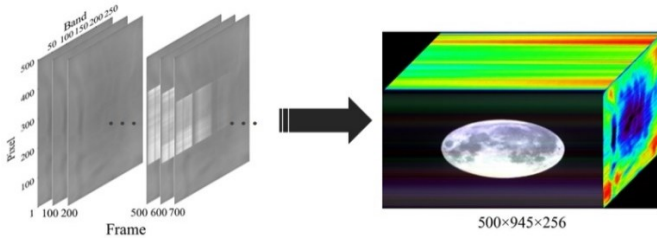

Fig. 4. The process of forming a data cube. Each image represents the response of 500 pixels in 256 bands. The data cube with size 500×945×256 is obtained by stitching the 945 frames together.

Our program has carried out several lunar observation experiments and selected eight of them illustrated in Fig. 5. The observation site was chosen at a sparsely populated high-altitude area with little pollution from urban light sources and a thin atmosphere. All experiments were observed on clear and cloudless nights with low atmospheric temperatures, irrespective of the effect of atmospheric radiation on hyperspectral imager signal reception [25]. Obviously, the elliptical moon measured by the spectrometer is a manifestation of oversampling, which is caused by a mismatch between the sampling frequency of the spectrometer and the relative angular velocity of the lunar motion [26]. Generated by the revolution of the moon, the angular velocity of the moon relative to the observation site is about 0.004°/s. The field of view of the spectrometer shown in Table 1 is 1°×0.002°, which ensures that there is no starlight interference in the field of view after aligning with the moon. To capture all the details of the moon, we set the frame rate to 4 fps and the integration time to 240ms. As a result, the lunar images presented in Fig. 5 have an oversampling ratio of around 2.
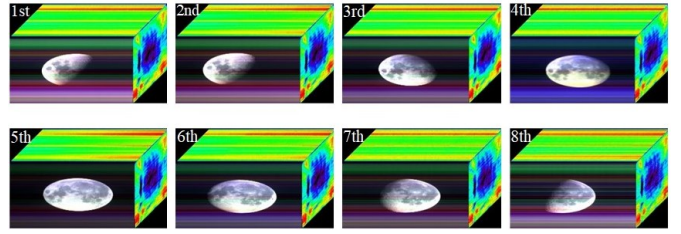

Fig. 5. Hyperspectral data cubes obtained from eight lunar observational experiments.

We further record the lunar phase angle and illuminated moon for each observation trial, as shown in Fig 6. The illuminated lunar area as seen from Earth is covered from 62.8% to 99.9%, based on a lunar phase angle in the range of 2.78-104.68°. The parameters aforementioned for each experiment are queried from GPL software Stellarium.
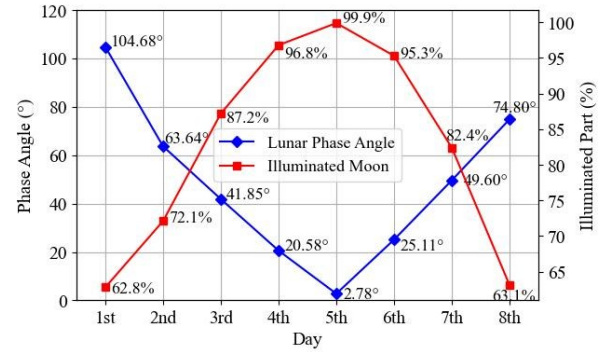

Fig. 6. Plot showing lunar phase angle and illuminated moon for each observation trial. The blue diamond blocks represent phase angles, and the red squares represent the proportions of the illuminated part.

3. DARK LEVEL CORRECTION METHOD

Measuring and removing the efforts from the dark level is important to give an accurate target response and clear texture of objects. From this point, we explored the dark level correction approach for each band individually. Firstly, a single-band image of the full moon is acquired by an imaging spectrometer, as shown in Fig. 7. The rows and columns of the image correspond to the sequence of pixels and frames in the experiment, respectively. Subsequently, we chose the band with a central wavelength of 1700nm due to the strong lunar radiation and weak atmospheric absorption in this band. Then, the transverse data is formed from the scan of the imaging spectrometer, and the longitudinal data depends on the slit of the spectrometer. The response R of spatial pixel w in the frame l can be expressed as:

$$R_{w,l} = I_{w,l} + B_w + DC_{w,l}(T) + RN \tag{1}$$

where $I_{w,l}$ is the response caused by the observed signal, B_w and $DC_{w,l}(T)$ are detector substrate and dark current respectively, and RN represents the random noise. $DC_{w,l}(T)$ is a function related to the ambient temperature T.
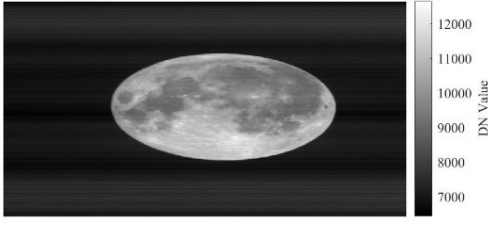
Fig. 7. Single-band grayscale image collected in the 5th experiment. The gray scale corresponds to the DN value.

A. Static dark level

Without the impacts from other light sources, the background around the moon is often considered to estimate the instrument's dark level since the signal strength in this area is comparable to Gaussian noise [8,14]. The observed response cold sky $R\_CS_{w,l}$ is given as:

$$R\_CS_{w,l} = B_w + DC_{w,l}(T) + N \tag{2}$$

$$N = I\_CS_{w,l} + RN \tag{3}$$

where N is the sum of the cold sky signal I_CS and random noise, which can be corrected by averaging multiple R_CS.

The cold sky signals used to estimate the dark level are the M columns selected in the red areas of Fig. 8. The dark level DS of the pixel w is given as:

$$DS_w(T\_M) = \frac{\sum_M R\_CS_{w,l}(T)}{M} \tag{4}$$

The temperature information T_M contained in $DS_w(T\_M)$ is only relevant to signals in selected M columns, which results in DS_w being static.
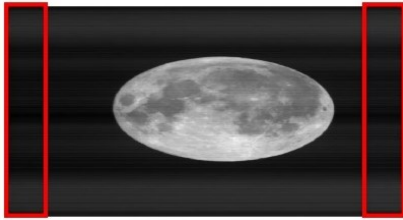

Fig. 8. Signal selection for estimating static dark level. The dark level value is estimated by the mean value of signals inside red solid boxes. The error using the bilateral area is smaller than that of the unilateral one [15].

B. Linear dark level

The dark level showed an upward trend during the observation, so using a static dark level for correction will cause incomplete and overcorrection signals in some columns. Establishing a dark level variation model based on cold sky signals at the start and end times will improve dark level accuracy. DSA_w and DSB_w are the static dark levels at the beginning and end of the observation, respectively.

$$DSA_w(T\_MA) = \frac{\sum_{MA} R\_CS_{w,l}(T)}{MA} \tag{5}$$

$$DSB_w(T\_MB) = \frac{\sum_{MB} R\_CS_{w,l}(T)}{MB} \tag{6}$$

where T_MA and T_MB represent the ambient temperature at the beginning and end of the observation, respectively.
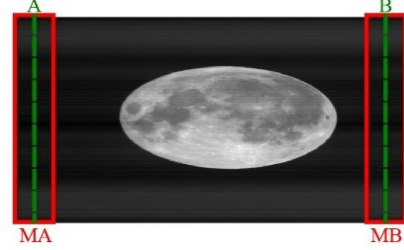

Fig. 9. Signal selection for estimating linear dark level. The dark level values of columns A and B are estimated by the mean value of signals inside red solid boxes MA and MB, respectively.

The linear dynamic dark level $DL_{w,l}$ of the pixel w in the column l is shown in Eq. (7) through Eq. (9):

$$DL_{w,l} = a_w \times l + b_w \tag{7}$$

$$a_w = \frac{DSB_w - DSA_w}{B - A} \tag{8}$$

$$b_w = DSA_w - a_w \times A \tag{9}$$

where a_w and b_w are the linear and constant parameters of the model.

C. Dynamic dark level

The dark level fluctuates at the beginning of the imaging spectrometer operation [14]. Hence, we design a dynamic model to fit the fluctuations of the dark level and correct the corresponding influences. Pixels that collect cold sky signals provide conditions for the establishment of dynamic models. All the pixels of the detector used the same material and process to keep the consistent trends of the dark level.

The overall workflow of the dynamic dark level correction approach is shown in Fig. 10. Our model includes three steps and the lunar image is the only input. Firstly, we randomly sampled the homogeneous areas from the cold sky around the target to estimate the spatial-dimensional static dark level. Meanwhile, rows of data are used to construct the trend of signal variation with time. Then, the dynamic dark level model covering the whole space and time is obtained by combining the static dark level and the time variation model. Finally, the dynamic dark level is subtracted from the original image to complete the correction process.
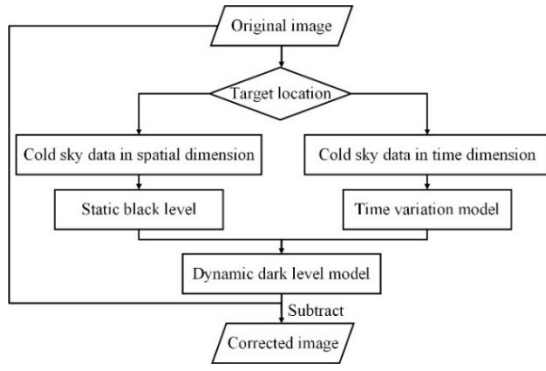
Fig. 10. Flow chart of the dynamic dark level correction.

As shown in Fig. 11, the cold sky signal on the left represents the response of all pixels during a part of the scanning time, while the signal on the upper side reflects the response of some pixels during the entire scanning process. Based on this, we proposed a new dynamic dark level correction method to solve the issues of dark level fluctuation.

Fig. 11. Signal selection for estimating dynamic dark level. The static dark level value is estimated by the mean value of signals inside the red box. The time variation model of the dark level is established by signals inside the blue dotted rectangle.

The static dark level $DS_w(T\_M)$ is defined by Eq. (4). Temperature variation TV defines the thermal dependencies for l, related to the temperature T_l, as expressed in Eq. (10):

$$TV_l(T\_l) = \frac{\sum_N R\_CS_{w,l}(T)}{N} \qquad (10)$$

For convenience, we normalize $TV_l(T\_l)$ to $TV_l'(T\_l)$, then the Eq. (10) can be modified as:

$$TV_l'(T\_l) = \frac{TV_l(T\_l) \times M}{\sum_M TV_l(T\_l)} \qquad (11)$$

The dynamic dark level $DD_{w,l}$ is defined as the matrix product of DS_w and TV_l':

$$DD_{w,l}(T\_l) = [DS_w(T\_M)]_{W \times 1}[TV_l'(T\_l)]_{1 \times L} \qquad (12)$$

where DD is a W × L matrix.

D. Evaluation index

To evaluate the effectiveness of the dynamic dark level correction method, the background proportion P_{bg} was introduced, which was defined as

$$P_{bg} = \left| \frac{S_{bg} \times N_{all}}{S_{all} \times N_{bg}} \right| \times 100\% \qquad (13)$$

where S_{bg} and N_{bg} represent the sum and number of pixels in the selected background area, respectively. Similarly, S_{all} and N_{all} denote the sum and number of pixels in the entire image.

Theoretically, when the value reaches 0, the dark level is completely removed. Obviously, a low value of metric P_{bg} indicates a better performance of dark level correction.

4. CORRECTION EFFECT EVALUATION

A. Experimental data

In our work, 100 columns of cold sky data were selected for estimating the dark level, considering the position and size of the Moon in Fig. 5 (250×530, the size of the whole image is 500×945). Specifically, the static dark level and linear dynamic dark level are calculated using 50 columns on the left side and right side, while the dynamic dark level is calculated using 100 columns on one side. For the dark level variation trend, we use data from 100 pixels above and below each.

B. Correction results

The dark level correction results of eight single-band images are shown in Fig. 12. To enhance the contrast of the image, final DN values are stretched from -120 to 270, and the corrected lunar backgrounds are shown in Fig. 11. The results are shown following: (1) all methods are effective in correcting dark levels. As shown in Fig. 12, the streaks caused by dark levels in the first column of images do not appear in subsequent images. All dark level corrected images of the moon are with a black homogeneous background; (2) the background in the static dark level correction result is heterogeneous. Negative values appear in the left background of Fig. 13(a), which indicates that the dark level is overcorrected. And the dark level on the right is not eliminated, especially in the fifth background; (3) the dynamic dark level model is closer to the true value of the dark level. The background around the moon in both linear dark level and dynamic dark level results is light blue and uniform (see Fig. 13(b) and 13(c)), which indicates that the background value is approximately zero.
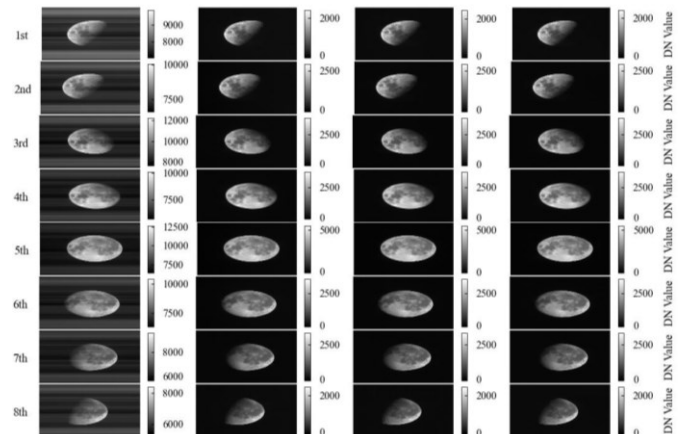
Fig.12. Results of dark level correction. From the first column to the fourth column, the listed images are the original single-band images, the corrected grayscale images of static dark level, linear dynamic dark level, and dynamic dark level, respectively.
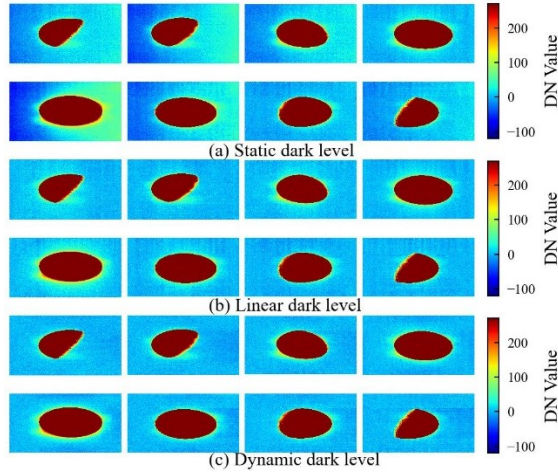

(a) Static dark level

(b) Linear dark level

(c) Dynamic dark level

Fig. 13. Results of dark level corrected background. The range of background DN values of lunar images is stretched from -120 to 270.

C. Metric evaluation

The size of the area used to calculate the background proportion P_{bg} is 10×10, and the positions of the center points are shown in Fig. 14, which are distributed around the moon. The selection of points follows the principle of the equidistant sampling method. To quantify the results of the dynamic dark level correction method for different wavelengths, we selected three bands in the short-wave infrared range, the central wavelengths of which are 1170nm, 1700nm, and 2202nm respectively. The background proportions of the lunar image in Fig.14 are listed in Table 2. It can be seen that: (1) static dark level only works well at P4 and P5. Particularly, the P_{bg} of P4 and P5 are less than 1% in 1170nm; (2) correction of static dark level will be less effective with increasing wavelength. The mean P_{bg} of static dark level in 2202nm reached 33.31%, which

means the lunar image has an extremely low signal-to-noise ratio; (3) the correction effect of dynamic dark level is generally better than that of linear dark level. The mean P_{bg} of the dynamic dark level is about 1 smaller than that of the linear dark level.
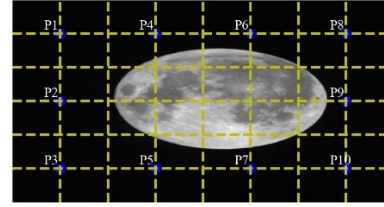

Fig. 14. Schematic diagram of the distribution of evaluation points. The image is divided into 6×8 small blocks, and the outer 10 intersection points are selected as evaluation points.

Fig. 15 summarizes the background proportion of 240 sets of dark level correction results, which were obtained from 10 evaluation points of 3 bands in 8 lunar images. Obviously, the correction of the static dark level is poor at the edges (see points 1,3,8,10 in Figure 15), while the other two methods have good results over the full range of the image. The dynamic spatial-time dark level correction approach performs the best among 169 sets of results, which accounts for more than 70%. As shown in Fig.16, the mean background proportions of our proposed approach are better than other approaches, and keep below 15% at 2202nm.
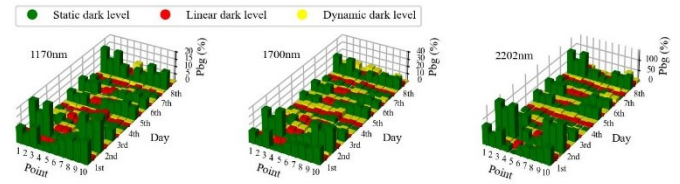

Fig. 15. Comparison of different dark level correction methods in 3 bands (1170nm, 1700nm, and 2202nm).

Table 2. Background proportion comparison of the lunar sing-band image (%)

| Band	Dark level	P1	P2	P3	P4	P5	P6	P7	P8	P9	P10	mean
1170nm	Static	6.84	4.97	6.63	0.44	0.74	6.75	6.77	7.91	10.37	7.83	5.93
	Linear	0.02	1.02	0.12	2.72	2.99	4.49	4.53	1.11	4.40	1.10	2.25
	Dynamic	0.04	0.76	0.16	1.02	1.13	1.78	1.52	0.56	2.80	0.17	1.00
1700nm	Static	10.20	7.86	10.37	1.38	0.85	10.41	10.38	12.42	15.18	13.25	9.23
	Linear	0.87	1.51	1.00	5.08	4.65	6.74	6.62	1.38	5.83	1.91	3.56
	Dynamic	0.25	0.53	0.43	2.19	1.28	2.78	1.78	0.82	2.86	0.41	1.33
2202nm	Static	46.88	36.86	44.13	10.51	6.28	20.27	24.98	46.40	48.76	48.03	33.31
	Linear	0.38	2.77	1.61	5.29	9.01	4.61	9.82	0.73	9.25	2.42	4.59
	Dynamic	0.98	0.61	0.21	1.25	3.81	0.32	3.23	0.03	0.84	0.45	1.17
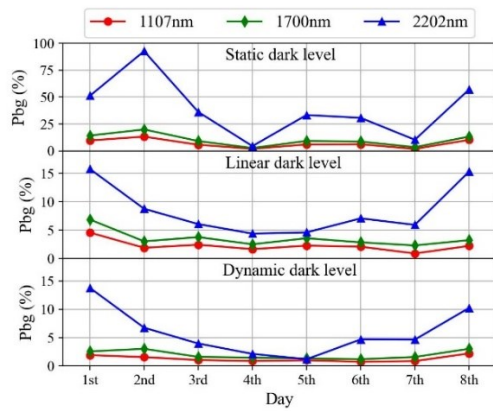
Fig. 16. Comparison of mean background proportion.

5. CONCLUSION

In this paper, we proposed a dynamic spatial-time method to correct the unstable background in lunar radiometric calibration processing. The method selects the monitored area and evaluates the dark level variation using inter-image element similarity. This method does not require additional equipment. Hence it can estimate the dark level of the lunar radiation data at any moment. The experiments showed that the proposed method could obtain a flat and clean lunar background. The mean background proportions of the full moon image were below 1.4%, and reached 1% at 1170 nm. The static dark level correction method gradually ineffective as the wavelength increased, while our proposed method can still effectively remove the dark level and improve the image quality.

In future work, we will consider combining our method with the observation of target radiation to further improve our method and apply it to other remote sensing image processing tasks. In addition, it is reasonable that non-target pixels can be reserved to improve the accuracy of infrared radiation data in the event of spectrometer dark level variations, where detector size is adequate.

Disclosures. The authors declare no conflicts of interest.

Data availability. Data underlying the results presented in this paper are available in Dataset 1.

References

1. S. Ma, Z. Zhou, Y. Zhang, Y. An, and G. Yang, "Identification of forest disturbance and estimation of forest age in subtropical mountainous areas based on Landsat time series data," Earth Science Informatics 2022 15:321-334 (2021).
2. M. F. Karim, and X. Zhang, "Analysis of Vegetative Cover Vulnerability in Rohingya Refugee Camps of Bangladesh Utilizing Landsat and Per Capita Greening Area (PCGA) Datasets," Remote Sensing 13(4922): 1-27 (2021).
3. M. Kan, W. Li, and J. Liu, "An Overview of the Application of High Resolution Satellite Remote Sensing Technique in Urban Planning and Management," Geomatics & Spatial Information Technology 35(S1): 100-102 (2012).
4. M. Zhang, F. Chen, H. Zhao, J. Wang, and N. Wang, "Recent Changes of Glacial Lakes in the High Mountain Asia and Its Potential Controlling Factors Analysis," Remote Sensing 13(3757):1-19 (2021).
5. X. Wang, A. Dou, X. Yuan, L. Ding, and X. Wang, "Application of HJ-2A/B Satellites in the Secondary Geological Disasters Recognition of Earthquakes," SPACECRAFT ENGINEERING 31(3): 195-203 (2022).
6. Y. Wu, J. LU, R. LIN, and X. Dang, "Research on standards for optical remote sensors of high-resolution earth observation satellite," Aerospace Standardization 2018(01): 4-9 (2018).
7. N. Lu, L. Ding, X. Zheng, X. Ye, C. Li, D. Lv, P. Zhang, X. Hu, C. Zhou, Z. You, J. Fang, J. Gong, X. Jiang, J. Li, L. Ma, N. Xu, "Introduction of the radiometric benchmark satellite being developed in China for remote sensing," Journal of Remote Sensing (Chinese) 24(6): 672-680 (2020).
8. H. H. Kieffer, and R. L. Wildey, "Establishing the Moon as a Spectral Radiance Standard," Atmosphere & Oceanic Technologies 13(2):360-375 (1996).
9. G. Paul, F. Nigel, L. Daniel and F. Jonathan, "The Traceable Radiometry Underpinning Terrestrial and Helio Studies (TRUTHS) mission," Proc. SPIE 9639, 1C (2015).
10. A. Angal, J. Mccorkel, and K. Thome, "Results from source-based and detector-based calibrations of a CLARREO calibration demonstration system," Proc. SPIE 9972, 06 (2016).
11. T. C. Stone, H. H. Kieffer, and K. J. Becker, "Modeling the Radiance of the Moon for On-orbit Calibration," Proc. SPIE 5151 (2003).
12. S. D. Miller, and R. E. Turner, "A Lunar Spectral Flux Database for Quantitative VIIRS Day/Night Band Environmental Applications," in Proceedings of the 4th Symposium on Future National Operational Environmental Satellites, pp. 20–24 January (2008).
13. D. Wang, "Research on Temperature Noise and Denoising of CMOS Image Sensor," Diss, Harbin Institute of Technology (2017).
14. Z. Li, T. Wei, and R. Zheng, "Design of black level calibration system for CMOS image sensor," in 2010 International Conference on Computer Application and System Modeling (ICCASM), pp. V10-643-647 (2010).
15. C. L. Dobbins, J. A. Dawson, and W. D. Edwards, "Compensation for instrument anomalies in imaging infrared measurements," Proc. SPIE 8706, 06 (2013).
16. J. Sun, X. Xiong, W. L. Barnes, and B. Guenther, "MODIS Reflective Solar Bands On-Orbit Lunar Calibration," IEEE Transactions on Geoscience & Remote Sensing 45(7): 2383-2393 (2007).
17. T. Wilson, A. Angal, A. Shrestha, and X. Xiong, "Lunar calibration improvements for the short-wave infrared bands in Aqua and Terra MODIS," Proc. SPIE 10423, 13 (2017).
18. T. Wilson, E. Aldoretta, A. Angal, X. Geng, K. Twedt, and X. Xiong, "Analysis of the on-orbit response-versus-scan-angle for the MODIS SWIR bands derived from lunar observations," Proc. SPIE 11530, 1E (2020).
19. R. Wu, P. Zhang, X. Zheng, X. Hu, N. Xu, L. Zhang, and Y. Qiao, "Data collection and irradiance conversion of lunar observation for MERSI," Optics and Precision Engineering 27(8): 1819-1827 (2019).
20. Y. Wang, "Study on Ground-based Spectral Imaging Measurement of the Moon and Lunar Radiometric Model," Diss, University of Chinese Academy of Sciences (2018).
21. C. Yong, D. Duan, C. Xu, and F. Chen, "The Study on the Dark Current of the Infrared Detector Measuring Method," Infrared Technology 34(4): 196-199 (2012).
22. J. Dong, X. Yang, and J. Dong, "Performance test and image processing of area CMOS image sensor," Infrared and Laser Engineering, 42(12): 3396-3401 (2013).
23. C. Lin, C Li, L. Wang, Y. Bi, and Y. Zheng, "Preflight spectral calibration of hyperspectral carbon dioxide spectrometer of TanSat," Infrared and Laser Engineering 25(8): 2064-2075 (2017).
24. Y. Wang, Y. Huang, S Wang, Z. Li, Z. Zhang, X. Hu, and P. Zhang, "Ground-based Observation System Development for the Moon Hyper-spectral Imaging," Publications of the Astronomical Society of the Pacific 129(975): 055002 (2017).
25. Y. Wang, Q. Zhu, J. Wang, and X. Zhuang, "Characterization of background radiation in SWIR hyperspectral imager," Journal of Infrared & Millimeter Waves 30(3): 279-283 (2011).

26. W. Wang, Y. Wang, L. An, C. Yu, and S. Wang, "Automatic observation and correction method of lunar hyperspectral image," Proc. SPIE 12178, 0G (2022).